Journal of Fluids and Structures 49 (2014) 242–262

Contents lists available at ScienceDirect

Journal of Fluids and Structures

journal homepage: www.elsevier.com/locate/jfs

Finite-depth effects on solitary waves in a floating ice sheet

Philippe Guyenne [a], Emilian I. Părău [b,*]

[a] Department of Mathematical Sciences, University of Delaware, DE 19716, USA
[b] School of Mathematics, University of East Anglia, Norwich NR4 7TJ, UK

ARTICLE INFO

Article history:
Received 11 April 2013
Accepted 28 April 2014
Available online 28 May 2014

Keywords:
Finite depth
Flexural-gravity waves
Hamiltonian theory
Solitary waves
Water waves

ABSTRACT

A theoretical and numerical study of two-dimensional nonlinear flexural-gravity waves propagating at the surface of an ideal fluid of finite depth, covered by a thin ice sheet, is presented. The ice-sheet model is based on the special Cosserat theory of hyperelastic shells satisfying Kirchhoff's hypothesis, which yields a conservative and nonlinear expression for the bending force. From a Hamiltonian reformulation of the governing equations, two weakly nonlinear wave models are derived: a 5th-order Korteweg–de Vries equation in the long-wave regime and a cubic nonlinear Schrödinger equation in the modulational regime. Solitary wave solutions of these models and their stability are analysed. In particular, there is a critical depth below which the nonlinear Schrödinger equation is of focusing type and thus admits stable soliton solutions. These weakly nonlinear results are validated by comparison with direct numerical simulations of the full governing equations. It is observed numerically that small- to large-amplitude solitary waves of depression are stable. Overturning waves of depression are also found for low wave speeds and sufficiently large depth. However, solitary waves of elevation seem to be unstable in all cases.

1. Introduction

In recent years, there has been renewed interest in the study of flexural-gravity (or hydroelastic) waves at the surface of a fluid covered by a thin elastic sheet, with applications to ocean waves interacting with sea ice in polar regions (Korobkin et al., 2011). A number of experiments have been performed with moving loads on ice, e.g. at McMurdo Sound, Antarctica, in deep water (Squire et al., 1996) and on Lake Saroma, Japan, in shallow water (Takizawa, 1985).

A theoretical challenge in this problem is to model the ice deformations subject to water wave motions, and thus a number of models have been proposed. The linear Euler–Bernoulli model for the ice sheet, combined with potential flow, has been widely used for small-amplitude water waves and ice deflections (Squire et al., 1996; Meylan and Sturova, 2009; Montiel et al., 2012; Mohapatra et al., 2013). However, reports of intense-in-ice events have highlighted limitations of linear theory (Marko, 2003) and, with the perspective of rougher sea conditions due to global warming (Squire, 2011), nonlinear theory has drawn increasing attention.

Nonlinear models based on Kirchhoff–Love plate theory have been adopted by a number of investigators (Forbes, 1986; Hegarty and Squire, 2008; Milewski et al., 2011). Recently, Plotnikov and Toland (2011) proposed a nonlinear formulation based on the special Cosserat theory for hyperelastic shells, which has the advantage of conserving elastic energy unlike the

* Corresponding author. Tel.: +44 1603592965.
E-mail address: e.parau@uea.ac.uk (E.I. Părău).

http://dx.doi.org/10.1016/j.jfluidstructs.2014.04.015

Kirchhoff–Love model. In this Cosserat framework, Milewski et al. (2011) performed a weakly nonlinear analysis of two-dimensional hydroelastic solitary waves on deep water using the multiple-scale method, while Guyenne and Părău (2012) examined the same problem both analytically and numerically through a Hamiltonian reformulation of the governing equations. In particular, both studies derived a defocusing nonlinear Schrödinger (NLS) equation implying the non-existence of small-amplitude solitary waves in the deep-water case.

The present paper extends the work of Guyenne and Părău (2012) to finite depth. Unlike infinite depth, there are two critical wave speeds: the minimum phase speed $c_{\min}$ and the long-wave (or shallow-water) limit c_0. In the past, this problem has been investigated through weakly nonlinear modelling (Haragus-Courcelle and Ilichev, 1998; Părău and Dias, 2002; Xia and Shen, 2002) and direct numerical simulations (Bonnefoy et al., 2009; Părău and Vanden-Broeck, 2011; Vanden-Broeck and Părău, 2011) using either the linear Euler–Bernoulli or nonlinear Kirchhoff–Love model for the ice sheet, combined with nonlinear potential flow. In particular, Xia and Shen (2002) derived a 5th-order Korteweg–de Vries (KdV) equation for two-dimensional hydroelastic waves on shallow water in the Euler–Bernoulli case, and Haragus-Courcelle and Ilichev (1998) derived a three-dimensional generalisation of the 5th-order KdV equation in a similar setting. Părău and Dias (2002) used Kirchhoff–Love plate theory and derived a stationary NLS equation for wave speeds c near $c_{\min}$. They found that this equation becomes focusing in shallow water and thus admits solitary wave solutions. More recently, Milewski and Wang (2013) proposed a Benney–Roskes–Davey–Stewartson system for three-dimensional weakly nonlinear hydroelastic waves on finite depth, based on the formulation of Plotnikov and Toland (2011).

Following Guyenne and Părău (2012), our starting point is the Hamiltonian formulation of the hydroelastic problem. The Dirichlet–Neumann operator is introduced to reduce the original Laplace problem to a lower-dimensional system involving quantities evaluated at the fluid–ice interface only. We restrict our attention to free solitary waves in two dimensions. Our weakly nonlinear analysis includes the derivation of a 5th-order KdV equation for c near c_0 and of a cubic NLS equation for c near $c_{\min}$, using the Hamiltonian perturbation approach of Craig et al. (2005a, 2010). We find that this NLS equation is of focusing type below a critical depth, similar to results of Părău and Dias (2002), and thus admits stable soliton solutions. Larger-amplitude waves for $c < c_{\min}$ are computed by solving the full steady equations with a boundary-integral method. Interestingly, their profiles can be well approximated by NLS solutions, despite being outside the regime of validity of the NLS equation. Both solitary waves of depression and elevation are found, including overturning waves of depression for c much lower than $c_{\min}$ and sufficiently large depth. For very shallow water, depression waves cannot reach a sufficiently high amplitude to overturn as they are bounded by the fluid depth.

The stability of these solitary waves is also investigated by performing direct numerical simulations in time with a high-order spectral method. Thanks to its analyticity properties, the Dirichlet–Neumann operator has a convergent Taylor series expansion in which each term can be determined recursively. This series expansion combined with the fast Fourier transform leads to an efficient and accurate numerical scheme for solving the full Hamiltonian equations. For $c < c_{\min}$, the stability of solitary waves of depression is confirmed by our time-dependent computations, while solitary waves of elevation seem to be unstable. For $c > c_0$, we observe solitary waves of elevation which compare well with generalised solitary wave solutions of our 5th-order KdV equation. Such waves however are inherently unstable because they continuously emit radiation and thus decay in time.

The remainder of the paper is organised as follows. Section 2 presents the mathematical formulation of the hydroelastic problem. The Dirichlet–Neumann operator is introduced and the Hamiltonian equations of motion are established. From this Hamiltonian formulation, the weakly nonlinear wave models are derived and analysed in Section 3. Section 4 describes the numerical methods to solve the full nonlinear problem for steady and unsteady waves. Numerical results are shown and discussed in Section 5. Finally, concluding remarks are given in Section 6.

2. Formulation

2.1. Equations of motion

We consider a two-dimensional fluid of uniform finite depth h beneath a continuous thin ice sheet. The fluid is assumed to be incompressible and inviscid, and the flow to be irrotational. The ice sheet is modelled using the special Cosserat theory of hyperelastic shells in Cartesian coordinates (Plotnikov and Toland, 2011), with the x-axis being the bottom of the ice sheet at rest and the y-axis directed vertically upwards. The vertical deformation of the ice is denoted by $y=\eta(x,t)$. The fluid velocity potential $\Phi(x,y,t)$ satisfies the Laplace equation

$$\nabla^2\Phi=0, \quad \text{for } x\in\mathbb{R}, \quad -h<y<\eta(x,t). \tag{1}$$

The nonlinear boundary conditions at $y=\eta(x,t)$ are the kinematic condition

$$\eta_t+\Phi_x\eta_x=\Phi_y, \tag{2}$$

and the dynamic condition

$$\Phi_t+\frac{1}{2}\left(\Phi_x^2+\Phi_y^2\right)+g\eta+P(x,t)+\frac{\mathcal{D}}{\rho}\left(\kappa_{ss}+\frac{1}{2}\kappa^3\right)=0, \tag{3}$$

where the subscripts are shorthand notation for partial/variational derivatives (e.g. $\Phi_t = \partial_t \Phi$), κ is the curvature of the fluid–ice interface and s is the arclength along this interface. In terms of η, the curvature is given by

$$\kappa = \frac{\eta_{xx}}{(1+\eta_x^2)^{3/2}},$$

and therefore

$$\kappa_{ss} + \frac{1}{2}\kappa^3 = \frac{1}{\sqrt{1+\eta_x^2}}\partial_x\left[\frac{1}{\sqrt{1+\eta_x^2}}\partial_x\left(\frac{\eta_{xx}}{(1+\eta_x^2)^{3/2}}\right)\right] + \frac{1}{2}\left(\frac{\eta_{xx}}{(1+\eta_x^2)^{3/2}}\right)^3.$$

The system is completed with the condition at the bottom,

$$\Phi_y = 0 \quad \text{at } y = -h. \tag{4}$$

Because we are only interested in localised disturbances and solitary waves in the present paper, we impose that the fluid velocity $\nabla\Phi$ as well as the ice deflection η and its derivatives tend to zero as $x \to \pm\infty$.

The constant $\mathcal{D}$ is the coefficient of flexural rigidity for the ice sheet, ρ the density of the fluid, g the acceleration due to gravity, and $P(x,t)$ the external pressure distribution exerted on the ice sheet. By definition, if $P > 0$, the pressure acts downwards. The dynamic condition (3) is obtained from the Bernoulli equation (Plotnikov and Toland, 2011). Since the wavelengths we consider are typically much larger than the ice thickness, we neglect the inertia of the thin ice sheet, hence the plate acceleration term is not included here. Schulkes et al. (1987) gave a physical justification for this approximation by the fact that the inertia of the moving water layer, which affects the water up to one wavelength in depth, is much larger than the inertia of the thin ice sheet. We also assume that the elastic plate is inextensible and not pre-stressed, and the tension due to plate stretching and bending is neglected.

If $P=0$, the total energy

$$H = \frac{1}{2}\int_{-\infty}^{\infty}\int_{-h}^{\eta} |\nabla\Phi|^2 \, dy\, dx + \frac{1}{2}\int_{-\infty}^{\infty}\left[g\eta^2 + \frac{\mathcal{D}}{\rho}\left(\frac{\eta_{xx}^2}{(1+\eta_x^2)^{5/2}}\right)\right] dx, \tag{5}$$

together with the impulse (or momentum)

$$I = \int_{-\infty}^{\infty}\int_{-h}^{\eta} \Phi_x \, dy\, dx,$$

and the volume (or mass)

$$V = \int_{-\infty}^{\infty} \eta \, dx, \tag{6}$$

are invariants of motion for (1)–(4). The first integral in (5) represents kinetic energy, while the second integral represents potential energy due to gravity and elasticity.

2.2. Hamiltonian formulation

In the case $P=0$, and following Zakharov (1968) and Craig and Sulem (1993), we can reduce the dimensionality of the Laplace problem (1)–(4) by introducing $\xi(x,t) = \Phi(x,\eta(x,t),t)$, the boundary values of the velocity potential on $y = \eta(x,t)$, together with the Dirichlet–Neumann operator (DNO)

$$G(\eta)\xi = (-\eta_x, 1)^\top \cdot \nabla\Phi|_{y=\eta}, \tag{7}$$

which is the singular integral operator that takes Dirichlet data ξ on $y = \eta(x,t)$, solves the Laplace equation (1) for Φ subject to (4), and returns the corresponding Neumann data (i.e. the normal fluid velocity there).

In terms of these boundary variables, Eqs. (1)–(4) can be rewritten as

$$\eta_t = G(\eta)\xi, \tag{8}$$

$$\xi_t = -\frac{1}{2(1+\eta_x^2)}\left[\xi_x^2 - (G(\eta)\xi)^2 - 2\xi_x\eta_x G(\eta)\xi\right] - g\eta - \frac{\mathcal{D}}{\rho}\left(\kappa_{ss} + \frac{1}{2}\kappa^3\right), \tag{9}$$

which are Hamiltonian equations for the canonically conjugate variables η and ξ, extending Zakharov's formulation of the water wave problem to hydroelastic waves on finite depth. Eqs. (8) and (9) have the canonical form

$$\begin{pmatrix}\eta_t \\ \xi_t\end{pmatrix} = \begin{pmatrix}0 & 1 \\ -1 & 0\end{pmatrix}\begin{pmatrix}H_\eta \\ H_\xi\end{pmatrix}, \tag{10}$$

whose Hamiltonian

$$H=\frac{1}{2}\int_{-\infty}^{\infty}\left[\xi G(\eta)\xi+g\eta^2+\frac{\mathcal{D}}{\rho}\left(\frac{\eta_{xx}^2}{(1+\eta_x^2)^{5/2}}\right)\right]dx, \tag{11}$$

corresponds to the total energy (5).

2.3. Dirichlet–Neumann operator

In light of its analyticity properties (Craig et al., 1997), the DNO can be expressed as a convergent Taylor series expansion

$$G(\eta)=\sum_{j=0}^{\infty}G_j(\eta), \tag{12}$$

where each term G_j can be determined recursively (Craig and Sulem, 1993; Xu and Guyenne, 2009). More specifically, for $j=2r>0$,

$$\begin{aligned}G_{2r}(\eta)=&\frac{1}{(2r)!}G_0(|D|^2)^{r-1}D\eta^{2r}D\\&-\sum_{s=0}^{r-1}\frac{1}{(2(r-s))!}(|D|^2)^{r-s}\eta^{2(r-s)}G_{2s}(\eta)\\&-\sum_{s=0}^{r-1}\frac{1}{(2(r-s)-1)!}G_0(|D|^2)^{r-s-1}\eta^{2(r-s)-1}G_{2s+1}(\eta),\end{aligned} \tag{13}$$

and, for $j=2r-1>0$,

$$\begin{aligned}G_{2r-1}(\eta)=&\frac{1}{(2r-1)!}(|D|^2)^{r-1}D\eta^{2r-1}D\\&-\sum_{s=0}^{r-1}\frac{1}{(2(r-s)-1)!}G_0(|D|^2)^{r-s-1}\eta^{2(r-s)-1}G_{2s}(\eta)\\&-\sum_{s=0}^{r-2}\frac{1}{(2(r-s-1))!}(|D|^2)^{r-s-1}\eta^{2(r-s-1)}G_{2s+1}(\eta),\end{aligned} \tag{14}$$

where $D=-\mathrm{i}\partial_x$ and $G_0=D\tanh(hD)$ are Fourier multiplier operators (D is defined in such a way that its Fourier symbol is k). In the infinite-depth limit $h\to\infty$, G_0 reduces to $|D|$ (Guyenne and Părău, 2012).

2.4. Linearised problem

The dispersion relation for the linearised problem is

$$c^2=\left(\frac{g}{k}+\frac{\mathcal{D}k^3}{\rho}\right)\tanh(hk), \tag{15}$$

where c is the phase speed and k the (positive) wavenumber. It can be shown that the phase speed $c(k)$ has a minimum $c_{\min}$ at $k=k_{\min}$ for any values of the parameters (see e.g. Squire et al., 1996; Părău and Dias, 2002). At this minimum, the phase velocity and group velocity are equal. Another critical speed in finite depth is the long-wave limit $c_0=\sqrt{gh}$ as $k\to0$.

3. Weakly nonlinear wave models

In this section, we analyse the weakly nonlinear regime for small- to moderate-amplitude waves. In finite depth, two asymptotic regimes are usually of interest: the long-wave regime and the modulational regime. In the former case, we derive a 5th-order KdV equation in the spirit of Haragus-Courcelle and Ilichev (1998) and Xia and Shen (2002), while in the latter case, we derive a cubic NLS equation in the spirit of Părău and Dias (2002). We emphasise again that these previous studies considered simplified models for the ice sheet. As in Guyenne and Părău (2012), we apply the Hamiltonian perturbation approach of Craig et al. (2005a, 2010), which is especially suitable for the present Hamiltonian formulation of the hydroelastic problem. An advantage of this approach is that it naturally associates a Hamiltonian to the equations of motion at each order of approximation. Changing variables through canonical transformations and expanding the Hamiltonian (11) are the main ingredients. Below we only give a brief description of the derivation of these weakly nonlinear models in the present context and refer the reader to Craig et al. (2005a, 2010) for further details.

3.1. Long-wave regime

3.1.1. Boussinesq system

To implement our derivation of the weakly nonlinear model in this regime, we use the long-wave scaling

$$X=\varepsilon x,\quad \eta=\varepsilon^2\tilde{\eta},\quad \xi=\varepsilon\tilde{\xi}, \tag{16}$$

where the small parameter $\varepsilon^2\sim(h/\ell_0)^2\sim a_0/h\ll 1$ is a measure of weak dispersion and nonlinearity (with a_0 and ℓ_0 being a characteristic wave height and wavelength respectively). Inserting (16) in the Hamiltonian (11) and expanding it in powers of ε up to order $O(\varepsilon^7)$, we find

$$\begin{aligned}H=\frac{\varepsilon^3}{2}\int_{-\infty}^{\infty}\Bigg[&h\xi_X^2+g\eta^2+\varepsilon^2\left(\eta\xi_X^2-\frac{h^3}{3}\xi_{XX}^2\right)\\&+\varepsilon^4\left(\frac{2}{15}h^5\xi_{XXX}^2-h^2\eta\xi_{XX}^2+\frac{\mathcal{D}}{\rho}\eta_{XX}^2\right)\Bigg]dX+O(\varepsilon^9),\end{aligned} \tag{17}$$

after dropping the tildes. In terms of $u=\xi_X$ (which plays the role of a horizontal interfacial velocity), the Hamiltonian (17) is expressed as

$$\begin{aligned}H=\frac{\varepsilon^3}{2}\int_{-\infty}^{\infty}\Bigg[&hu^2+g\eta^2+\varepsilon^2\left(\eta u^2-\frac{h^3}{3}u_X^2\right)\\&+\varepsilon^4\left(\frac{2}{15}h^5u_{XX}^2-h^2\eta u_X^2+\frac{\mathcal{D}}{\rho}\eta_{XX}^2\right)\Bigg]dX+O(\varepsilon^9).\end{aligned} \tag{18}$$

There is also a change in symplectic form associated with (16), so that Eq. (10) is transformed to

$$\begin{pmatrix}\eta_t\\u_t\end{pmatrix}=\varepsilon^{-2}\begin{pmatrix}0&-\partial_X\\-\partial_X&0\end{pmatrix}\begin{pmatrix}H_\eta\\H_u\end{pmatrix}.$$

These equations constitute a high-order Boussinesq system in the present problem and read more explicitly

$$\begin{aligned}\eta_\tau&=-\partial_X\left[hu+\varepsilon^2\left(\eta u+\frac{h^3}{3}u_{XX}\right)+\varepsilon^4\left(\frac{2}{15}h^5u_{XXXX}+h^2(\eta u_X)_X\right)\right],\\u_\tau&=-\partial_X\left[g\eta+\frac{\varepsilon^2}{2}u^2+\varepsilon^4\left(\frac{\mathcal{D}}{\rho}\eta_{XXXX}-\frac{h^2}{2}u_X^2\right)\right],\end{aligned}$$

where $\tau=\varepsilon t$ is a long time scale. Up to order $O(\varepsilon^2)$, this is the usual Hamiltonian Boussinesq system of the water wave problem without flexural effects (Kaup, 1975).

3.1.2. Fifth-order KdV equation

Furthermore, by framing the Boussinesq system in characteristic coordinates

$$\begin{pmatrix}r\\s\end{pmatrix}=\begin{pmatrix}\left(\frac{g}{4h}\right)^{1/4}&\left(\frac{h}{4g}\right)^{1/4}\\\left(\frac{g}{4h}\right)^{1/4}&-\left(\frac{h}{4g}\right)^{1/4}\end{pmatrix}\begin{pmatrix}\eta\\u\end{pmatrix}, \tag{19}$$

we obtain

$$\begin{aligned}H=\frac{\varepsilon^3}{2}\int_{-\infty}^{\infty}\Bigg[&\sqrt{gh}(r^2+s^2)+\varepsilon^2\left\{\frac{1}{2\sqrt{2}}\left(\frac{g}{h}\right)^{1/4}(r^3-r^2s-rs^2+s^3)\right.\\&\left.-\frac{h^3}{6}\sqrt{\frac{g}{h}}(r_X^2-2r_Xs_X+s_X^2)\right\}+\varepsilon^4\left\{\frac{h^5}{15}\sqrt{\frac{g}{h}}(r_{XX}^2-2r_{XX}s_{XX}+s_{XX}^2)\right.\\&-\frac{h^2}{2\sqrt{2}}\left(\frac{g}{h}\right)^{1/4}(rr_X^2-2rr_Xs_X+rs_X^2+sr_X^2-2sr_Xs_X+ss_X^2)\\&\left.+\frac{\mathcal{D}}{2\rho}\sqrt{\frac{h}{g}}(r_{XX}^2+2r_{XX}s_{XX}+s_{XX}^2)\right\}\Bigg]dX+O(\varepsilon^9),\end{aligned} \tag{20}$$

where r and s are principally right- and left-moving components of the solution, respectively, which obey the evolution equations

$$\begin{pmatrix}r_t\\s_t\end{pmatrix}=\varepsilon^{-2}\begin{pmatrix}-\partial_X&0\\0&\partial_X\end{pmatrix}\begin{pmatrix}H_r\\H_s\end{pmatrix}.$$

The Hamiltonian (20) can be further reduced by subtracting a multiple of the impulse

$$I=\int_{-\infty}^{\infty}\eta\xi_x\,dx=\frac{\varepsilon^3}{2}\int_{-\infty}^{\infty}(r^2-s^2)\,dX,$$

and by restricting our attention to right-moving solutions r in a region of phase space where $s\le O(\varepsilon^4)$. As a result, the new Hamiltonian takes the form

$$\begin{aligned}\tilde{H}&=H-c_0I,\\&=\frac{\varepsilon^5}{2}\int_{-\infty}^{\infty}\left[\frac{1}{2\sqrt{2}}\left(\frac{g}{h}\right)^{1/4}r^3-\frac{h^3}{6}\sqrt{\frac{g}{h}}r_X^2\right.\\&\quad\left.+\varepsilon^2\left\{\left(\frac{h^5}{15}\sqrt{\frac{g}{h}}+\frac{\mathcal{D}}{2\rho}\sqrt{\frac{h}{g}}\right)r_{XX}^2-\frac{h^2}{2\sqrt{2}}\left(\frac{g}{h}\right)^{1/4}rr_X^2\right\}\right]dX+O(\varepsilon^9),\end{aligned}$$

and the evolution equation for r becomes

$$r_t=-\varepsilon^2\partial_X\tilde{H}_r,$$

which is expressed in a reference frame moving at speed c_0 (as a result of the subtraction of c_0I from H). More explicitly, this yields the 5th-order KdV equation

$$r_\tau+3c_2rr_X+c_3r_{XXX}+2\varepsilon^2c_4r_Xr_{XX}+\varepsilon^2c_4rr_{XXX}+\varepsilon^2c_5r_{XXXXX}=0,\tag{21}$$

where $\tau=\varepsilon^3t$,

$$c_2=\frac{1}{2\sqrt{2}}\left(\frac{g}{h}\right)^{1/4},\quad c_3=\frac{h^3}{6}\sqrt{\frac{g}{h}},\quad c_4=\frac{h^2}{2\sqrt{2}}\left(\frac{g}{h}\right)^{1/4},\quad c_5=\frac{h^5}{15}\sqrt{\frac{g}{h}}+\frac{\mathcal{D}}{2\rho}\sqrt{\frac{h}{g}},$$

and the corresponding Hamiltonian (with respect to τ) reads

$$H=\frac{1}{2}\int\left[c_2r^3-c_3r_X^2-\varepsilon^2c_4rr_X^2+\varepsilon^2c_5r_{XX}^2\right]dX.$$

Note that the coefficients c_2, c_3, c_4 and c_5 are all positive. This Hamiltonian 5th-order KdV equation is similar to those investigated by Craig and Groves (1994) and Champneys et al. (2002) in the context of gravity and gravity-capillary water waves, respectively. However, there are significant differences from the 5th-order KdV equations derived by Haragus-Courcelle and Ilichev (1998) and Xia and Shen (2002) for hydroelastic waves, which do not have the high-order nonlinear terms in factor of c_4.

At this order of approximation, the ice-sheet deflection is given in terms of r by

$$\eta(X,\tau)=\varepsilon^2\left(\frac{h}{4g}\right)^{1/4}r(X,\tau),\tag{22}$$

after inverting (19).

3.1.3. Solitary wave solutions

Because Eq. (21) is not exactly integrable in general, it is solved numerically for solitary waves which are stationary in a secondary reference frame moving at constant speed σ. In our Hamiltonian framework, these solutions correspond to fixed points of the variational $\delta_r(H-\sigma I/\varepsilon^3)$. This leads to the nonlinear ordinary differential equation

$$-\sigma r+\frac{3}{2}c_2r^2+c_3r_{XX}+\varepsilon^2c_4(rr_X)_X-\frac{\varepsilon^2}{2}c_4r_X^2+\varepsilon^2c_5r_{XXXX}=0,\tag{23}$$

which is discretised by a pseudospectral method assuming periodic boundary conditions, as described in Section 4. Eq. (23) is solved iteratively by Newton's method using the classical KdV soliton

$$r(X)=\frac{\sigma}{c_2}\operatorname{sech}^2\left(\frac{1}{2}\sqrt{\frac{\sigma}{c_3}}X\right),\tag{24}$$

as an initial guess. A number of 1024 grid points is typically specified in these computations. Results will be presented in Section 4.

3.2. Modulational regime

3.2.1. Canonical transformations

In this regime, the first step is a normal mode decomposition defined by

$$\eta=\frac{1}{\sqrt{2}}a^{-1}(D)(z+\overline{z})+\tilde{\eta},\quad\tilde{\eta}=\mathbb{P}_0\eta,$$

$$\xi = \frac{1}{\sqrt{2}\mathrm{i}}\, a(D)(z-\overline{z}) + \tilde{\xi}, \quad \tilde{\xi} = \mathbb{P}_0\xi, \tag{25}$$

where

$$a(D) = \sqrt[4]{\frac{g+\mathcal{D}D^4/\rho}{G_0}},$$

and $(\tilde{\eta},\tilde{\xi})$ are the zeroth modes representing the mean flow. The overbar represents complex conjugation, and $\mathbb{P}_0$ is the projection that associates to (η,ξ) their zeroth-frequency components. The zeroth modes are split from the higher ones in this decomposition because otherwise the change of variables $(\eta,\xi)\to(z,\overline{z})$ is not invertible due to the fact that $a^{-1}(0)=0$ for $k=0$. As a result, the canonical system (10) is transformed to

$$\begin{pmatrix} z_t \\ \overline{z}_t \\ \tilde{\eta}_t \\ \tilde{\xi}_t \end{pmatrix} = \begin{pmatrix} 0 & -\mathrm{i}(\mathbb{I}-\mathbb{P}_0) & 0 & 0 \\ \mathrm{i}(\mathbb{I}-\mathbb{P}_0) & 0 & 0 & 0 \\ 0 & 0 & 0 & \mathbb{P}_0 \\ 0 & 0 & -\mathbb{P}_0 & 0 \end{pmatrix} \begin{pmatrix} H_z \\ H_{\overline{z}} \\ H_{\tilde{\eta}} \\ H_{\tilde{\xi}} \end{pmatrix},$$

where $\mathbb{I}$ is the identity operator.

The next step introduces the modulational Ansatz

$$z = \varepsilon u(X,t)\mathrm{e}^{\mathrm{i}k_0x}, \quad \overline{z} = \varepsilon\overline{u}(X,t)\mathrm{e}^{-\mathrm{i}k_0x}, \tag{26}$$

$$\tilde{\eta} = \varepsilon^2\tilde{\eta}_1(X,t), \quad \tilde{\xi} = \varepsilon\tilde{\xi}_1(X,t), \tag{27}$$

which implies that we look for solutions in the form of quasi-monochromatic waves with carrier wavenumber $k_0>0$ and with slowly varying amplitude depending on $X=\varepsilon x$. Wave steepness is measured by the small parameter $\varepsilon\sim k_0a_0\ll 1$ where a_0 is a characteristic wave amplitude. Here the definition of ε is different from that in Section 3.1 but we use the same notation for convenience. The corresponding equations of motion read

$$\begin{pmatrix} u_t \\ \overline{u}_t \\ \tilde{\eta}_{1t} \\ \tilde{\xi}_{1t} \end{pmatrix} = \begin{pmatrix} 0 & -\mathrm{i}\varepsilon^{-1} & 0 & 0 \\ \mathrm{i}\varepsilon^{-1} & 0 & 0 & 0 \\ 0 & 0 & 0 & \varepsilon^{-2} \\ 0 & 0 & -\varepsilon^{-2} & 0 \end{pmatrix} \begin{pmatrix} H_u \\ H_{\overline{u}} \\ H_{\tilde{\eta}_1} \\ H_{\tilde{\xi}_1} \end{pmatrix}. \tag{28}$$

3.2.2. Expansion of the Hamiltonian

The modulational Ansatz (26)–(27) also introduces the small parameter ε in the expression of the Hamiltonian (11) which can then be expanded in powers of ε. Up to order $O(\varepsilon^3)$, we find

$$\begin{aligned} H = \frac{\varepsilon}{2}\int_{-\infty}^{\infty} \Big[& \overline{u}\Big(\omega(k_0) + \varepsilon\omega_k(k_0)D_X + \frac{\varepsilon^2}{2}\omega_{kk}(k_0)D_X^2\Big)u + \text{c.c.} \\ & + \varepsilon^2\Big\{\frac{1}{2}G_0(k_0)\Big(G_0(k_0)G_0(2k_0) - k_0^2\Big) - \frac{5\mathcal{D}}{4\rho}k_0^6a^{-4}(k_0)\Big\}|u|^4 \\ & + \varepsilon^2(2\mathrm{i}k_0D_X\tilde{\xi}_1 + \{k_0^2 - G_0^2(k_0)\}a^2(k_0)\tilde{\eta}_1)|u|^2 \\ & + \varepsilon^2(h\tilde{\xi}_1D_X^2\tilde{\xi}_1 + g\tilde{\eta}_1^2)\Big]\,dX + O(\varepsilon^4), \end{aligned} \tag{29}$$

where c.c. stands for the complex conjugate of all the preceding terms on the right-hand side of the equation, and the coefficient

$$\omega(k) = \sqrt{G_0(g+\mathcal{D}k^4/\rho)},$$

denotes the linear dispersion relation in terms of the angular frequency. The scale separation lemma of Craig et al. (2005b) is used to homogenise the fast oscillations in x and retain the four-wave resonant terms (see also Craig et al., 2012). Note the mean-flow contributions to this order of approximation in (29).

As in the long-wave regime, the Hamiltonian (29) can be further reduced by subtracting a multiple of the wave action

$$M = \varepsilon\int_{-\infty}^{\infty}|u|^2\,dX, \tag{30}$$

together with a multiple of the impulse

$$I = \varepsilon\int_{-\infty}^{\infty}\Big[k_0|u|^2 + \frac{\varepsilon}{2}(\overline{u}D_Xu + u\overline{D_Xu}) + \mathrm{i}\varepsilon^2\tilde{\eta}_1D_X\tilde{\xi}_1\Big]\,dX + O(\varepsilon^4),$$

so that it simplifies to

$$\begin{aligned}\tilde{H} &= H-\omega_k(k_0)I-(\omega(k_0)-k_0\omega_k(k_0))M,\\ &=\frac{\varepsilon^3}{2}\int_{-\infty}^{\infty}\Big[\omega_{kk}(k_0)\overline{u}D_X^2u+\Big\{\frac{1}{2}G_0(k_0)\Big(G_0(k_0)G_0(2k_0)-k_0^2\Big)-\frac{5\mathcal{D}}{4\rho}k_0^6a^{-4}(k_0)\Big\}|u|^4\\ &\quad+\{2\mathrm{i}k_0D_X\tilde{\xi}_1+(k_0^2-G_0^2(k_0))a^2(k_0)\tilde{\eta}_1\}|u|^2\\ &\quad+h\tilde{\xi}_1D_X^2\tilde{\xi}_1+g\tilde{\eta}_1^2-2\mathrm{i}\omega_k(k_0)\tilde{\eta}_1D_X\tilde{\xi}_1\Big]dX+O(\varepsilon^4).\end{aligned}\tag{31}$$

The subtraction of a multiple of M from H reflects the fact that our approximation to the problem is phase invariant, while the subtraction of $\omega_k(k_0)I$ is equivalent to changing the coordinate system into a reference frame moving with the group velocity $\omega_k(k_0)$.

3.2.3. NLS equation

Accordingly, Eq. (28) takes the reduced form

$$\begin{aligned}\mathrm{i}u_\tau &= \frac{1}{2}\omega_{kk}(k_0)D_X^2u+\Big[\frac{1}{2}G_0(k_0)\Big(G_0(k_0)G_0(2k_0)-k_0^2\Big)-\frac{5\mathcal{D}}{4\rho}k_0^6a^{-4}(k_0)\Big]u|u|^2\\ &\quad+\Big[\mathrm{i}k_0D_X\tilde{\xi}_1+\frac{1}{2}\Big(k_0^2-G_0^2(k_0)\Big)a^2(k_0)\tilde{\eta}_1\Big]u,\end{aligned}\tag{32}$$

$$\varepsilon\tilde{\eta}_{1\,\tau}=-\mathrm{i}k_0D_X|u|^2+hD_X^2\tilde{\xi}_1+\mathrm{i}\omega_k(k_0)D_X\tilde{\eta}_1,\tag{33}$$

$$\varepsilon\tilde{\xi}_{1\,\tau}=-\frac{1}{2}\Big(k_0^2-G_0^2(k_0)\Big)a^2(k_0)|u|^2+\mathrm{i}\omega_k(k_0)D_X\tilde{\xi}_1-g\tilde{\eta}_1,\tag{34}$$

where $\tau=\varepsilon^2t$. To leading order in ε, the right-hand side of (33) equals zero. Then integrating this equation with respect to X assuming vanishing conditions at infinity (as is the case for solitary waves), we obtain

$$\mathrm{i}k_0|u|^2-hD_X\tilde{\xi}_1-\mathrm{i}\omega_k(k_0)\tilde{\eta}_1=0.\tag{35}$$

Similarly, from (34), we have

$$\frac{1}{2}\Big(k_0^2-G_0^2(k_0)\Big)a^2(k_0)|u|^2-\mathrm{i}\omega_k(k_0)D_X\tilde{\xi}_1+g\tilde{\eta}_1=0.\tag{36}$$

Solving (35) and (36) for $D_X\tilde{\xi}_1$ and $\tilde{\eta}_1$ leads to

$$D_X\tilde{\xi}_1=-\frac{\mathrm{i}}{h}\Big[\frac{\omega_k^2(k_0)}{h}-g\Big]^{-1}\Big[gk_0+\frac{1}{2}\omega_k(k_0)\Big(k_0^2-G_0^2(k_0)\Big)a^2(k_0)\Big]|u|^2,\tag{37}$$

and

$$\tilde{\eta}_1=\Big[\frac{\omega_k^2(k_0)}{h}-g\Big]^{-1}\Big[\frac{1}{2}\Big(k_0^2-G_0^2(k_0)\Big)a^2(k_0)+\frac{k_0\omega_k(k_0)}{h}\Big]|u|^2.\tag{38}$$

Finally, substituting (37) and (38) into (32) results in the NLS equation

$$\mathrm{i}u_\tau+\lambda u_{XX}+\mu|u|^2u=0,\tag{39}$$

whose coefficients are given by

$$\lambda=\frac{1}{2}\omega_{kk}(k_0),\tag{40}$$

$$\begin{aligned}\mu &= \frac{1}{2}G_0(k_0)\Big(k_0^2-G_0(k_0)G_0(2k_0)\Big)+\frac{5\mathcal{D}}{4\rho}k_0^6a^{-4}(k_0)\\ &\quad+\frac{k_0}{h}\Big[g-\frac{\omega_k^2(k_0)}{h}\Big]^{-1}\Big[gk_0+\frac{1}{2}\omega_k(k_0)\Big(k_0^2-G_0^2(k_0)\Big)a^2(k_0)\Big]\\ &\quad+\frac{1}{2}\Big(k_0^2-G_0^2(k_0)\Big)a^2(k_0)\Big[g-\frac{\omega_k^2(k_0)}{h}\Big]^{-1}\Big[\frac{1}{2}\Big(k_0^2-G_0^2(k_0)\Big)a^2(k_0)+\frac{k_0\omega_k(k_0)}{h}\Big],\end{aligned}\tag{41}$$

and the corresponding Hamiltonian is

$$H=\int_{-\infty}^{\infty}\Big(\lambda|u_X|^2-\frac{\mu}{2}|u|^4\Big)\,dX.\tag{42}$$

According to (25), the ice-sheet deflection can be expressed in terms of u as

$$\eta(X,\tau)=\frac{\varepsilon}{\sqrt{2}}\left[\sqrt[4]{\frac{(k_0+\varepsilon D_X)\tanh(h(k_0+\varepsilon D_X))}{g+\mathcal{D}(k_0+\varepsilon D_X)^4/\rho}}\,u(X,\tau)\mathrm{e}^{\mathrm{i}k_0X/\varepsilon}+\text{c.c.}\right]+\varepsilon^2\tilde{\eta}_1, \tag{43}$$

where the mean component $\tilde{\eta}_1$ is given by (38).

3.2.4. Envelope soliton solutions

Eq. (39) is of focusing type, and thus admits stable solitary wave solutions travelling at the group velocity $\omega_k(k_0)$, if $\lambda\mu>0$ (Grillakis et al., 1987). In infinite depth, we found that $\lambda\mu<0$ when $k_0=k_{\min}$. However, in finite depth, λ is always positive for $k_0=k_{\min}$, while the sign of μ depends on the depth h. There exists a critical depth h_c where $\mu=0$, implying that higher-order terms need to be included in the equation. We will not consider this higher-order situation here. For $h>h_c$, the coefficient μ is negative and Eq. (39) is defocusing, which is consistent with results found in the infinite-depth limit (Milewski et al., 2011; Guyenne and Părău, 2012). For $h<h_c$, the coefficient μ is positive and thus Eq. (39) admits solitary wave solutions.

Considering Takizawa's experiments on Lake Saroma, Japan (Takizawa, 1985), the ice-sheet thickness was 0.17 m and the water depth was 6.8 m. Flexural-gravity waves were generated by moving a load (ski-doo snowmobile) at various speeds on top of the ice sheet. Wavelengths of the order of 10 m were observed. The graphs of λ and μ for the conditions in Takizawa's experiments are presented in Fig. 1, which indicates that $h_c=19.3$ m for the present model. In Părău and Dias (2002), the analysis of a stationary NLS equation derived for a simplified model of the ice sheet showed that the change from focusing to defocusing occurs at a different but comparable critical depth $h_c=16.8$ m.

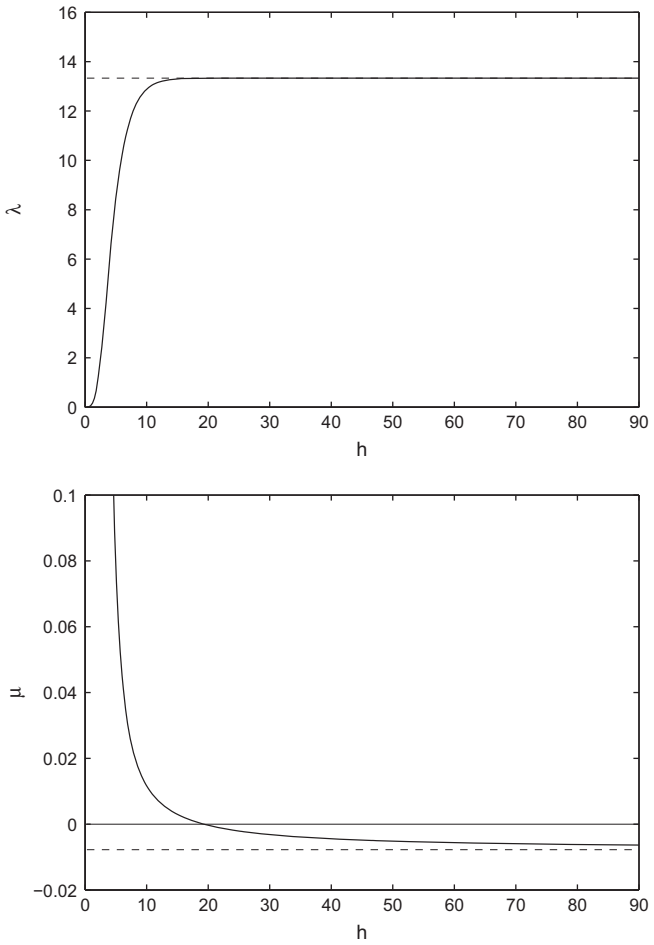

Fig. 1. NLS coefficients λ (top figure, solid line) and μ (bottom figure, solid line) as given by (40) and (41) for Takizawa's experiments on Lake Saroma (Takizawa, 1985). The corresponding values $\lambda=13.33$ and $\mu=-0.0078$ in the infinite-depth limit (see Eqs. (3.19) and (3.20) in Guyenne and Părău, 2012) are represented by a dashed line. The depth units are in metres.

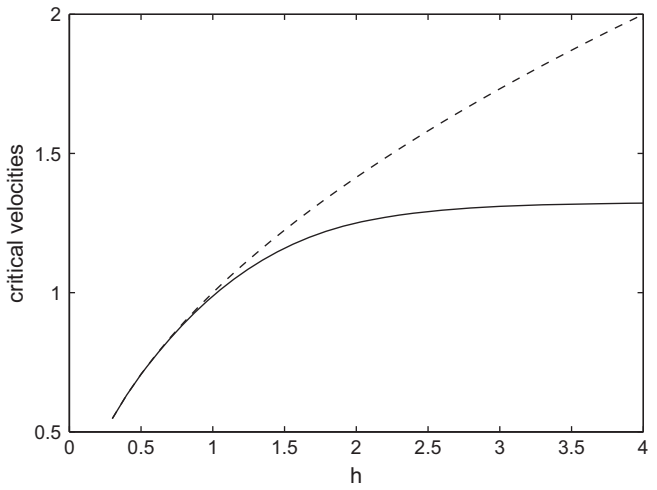

Fig. 2. $c_{\min}$ (solid line) and c_0 (dashed line) as functions of h.

In view of comparing with (steady) fully nonlinear solutions, as discussed in the next section, we consider the exact NLS soliton

$$u(X,\tau)=\sqrt{2}u_0\,\mathrm{sech}\left(u_0\sqrt{\frac{\mu}{\lambda}}X\right)\mathrm{e}^{\mathrm{i}\mu u_0^2\tau}, \tag{44}$$

which corresponds to solitary waves whose crests are stationary relative to their envelopes (Akylas, 1993).

We point out that the mean components (37) and (38), and hence the NLS equation (39) together with its solution (44), are well-defined provided the group velocity $\omega_k(k_0)$ does not equal the long-wave limit $c_0=\sqrt{gh}$. For $k_0=k_{\min}$, Fig. 2 reveals that $c_{\min}=\omega_k(k_{\min})\to c_0$ as $h\to 0$. Therefore, the long-wave regime tends to be the best-suited asymptotic regime in the shallow-water limit, as could be expected.

4. Numerical methods

Following Takizawa (1985), Bonnefoy et al. (2009) and Milewski et al. (2011), we non-dimensionalise (1)–(4) using the characteristic scales

$$\mathcal{L}=\left(\frac{\mathcal{D}}{\rho g}\right)^{1/4},\quad \mathcal{V}=\left(\frac{\mathcal{D}g^3}{\rho}\right)^{1/8},$$

as unit length and unit velocity, respectively. In dimensionless form, these equations read

$$\nabla^2\Phi=0,\quad \text{for } -h<y<\eta(x,t), \tag{45}$$

$$\eta_t+\Phi_x\eta_x=\Phi_y,\quad \text{for } y=\eta(x,t), \tag{46}$$

$$\Phi_t+\frac{1}{2}\left(\Phi_x^2+\Phi_y^2\right)+\eta+P+\kappa_{ss}+\frac{1}{2}\kappa^3=0,\quad \text{for } y=\eta(x,t), \tag{47}$$

$$\Phi_y=0,\quad \text{at } y=-h. \tag{48}$$

Since we are interested in solitary waves, the key parameters which are examined in the problem are the dimensionless wave speed c and the dimensionless water depth h. The dimensionless value of the critical depth in our NLS regime is $h_c=8.773$ which is comparable to the value $h_c=7.63$ obtained by Părău and Dias (2002) in the Kirchhoff–Love case. We note that Milewski and Wang (2013) found the critical depth to be $h_c\approx 233$ for the same Cosserat ice-sheet model but with a different analysis.

For the experiments on Lake Saroma (Takizawa, 1985), we obtain $h=3.095$ and $c_{\min}=1.3118$ while $c_0=1.7592$. By comparison, $c_{\min}=2/3^{3/8}=1.3247$ in infinite depth. Fig. 2 indicates that c_0 becomes increasingly higher than $c_{\min}$ as h increases.

To compute fully nonlinear steady and unsteady waves, we use a boundary-integral method (combined with Cauchy's integral formula) and a high-order spectral method, respectively. These extend the methods presented in Guyenne and Părău (2012) to finite depth, and therefore the reader is referred to this paper for further details.

4.1. Boundary-integral method for steady waves

For steady waves in a reference frame moving at constant speed c, the complex potential

$$w(z)=\Phi(x,y)+\mathrm{i}\Psi(x,y), \tag{49}$$

is introduced in the fluid domain, where $\Psi(x,y)$ is the stream function. The physical plane

$$z=x(w)+\mathrm{i}y(w),$$

is mapped to $w(z)$ in the inverse plane. Therefore

$$\Phi_x-\mathrm{i}\Phi_y=\frac{dw}{dz}=\frac{1}{x_\Phi+\mathrm{i}y_\Phi}.$$

Without loss of generality, we set $\Psi=0$ on the fluid–ice interface and choose $\Phi=0$ at $x=0$. It can be shown that $\Psi=-ch$ on the bottom. In terms of the potential, the fluid–ice interface is parameterised by

$$(x(\Phi),y(\Phi))=(x(\Phi+\mathrm{i}0),y(\Phi+\mathrm{i}0)).$$

In this notation, $x'(\Phi)$ and $y'(\Phi)$ are the values of x_Φ and y_Φ evaluated at the interface $\Psi=0$. As $y_\Phi=0$ on the bottom $\Psi=-ch$, we can extend the function $x_\Phi-1/c+\mathrm{i}y_\Phi$ by symmetry about the line $\Psi=-ch$ to an analytic function in the strip $(-2ch,0)$.

The main difference in the steady case between the finite- and infinite-depth problems is that we apply the Cauchy integral formula along a rectangular strip between $\Psi=0$ and $\Psi=-2ch$. Assuming the symmetry of solutions about $\Phi=0$, application of the Cauchy integral formula yields, after some algebra,

$$\begin{aligned}x'(\Phi_0)-\frac{1}{c}=&-\frac{1}{\pi}\int_0^\infty y'(\Phi)\left(\frac{1}{\Phi-\Phi_0}+\frac{1}{\Phi+\Phi_0}\right)d\Phi\\&+\frac{1}{\pi}\int_0^\infty\frac{(\Phi_0-\Phi)y'(\Phi)+2ch(x'(\Phi)-1/c)}{(\Phi-\Phi_0)^2+4c^2h^2}d\Phi\\&+\frac{1}{\pi}\int_0^\infty\frac{-(\Phi_0+\Phi)y'(\Phi)+2ch(x'(\Phi)-1/c)}{(\Phi+\Phi_0)^2+4c^2h^2}d\Phi,\end{aligned} \tag{50}$$

where the primes denote differentiation with respect to Φ. The evaluation point Φ_0 lies on the interface and the first integral on the right-hand side is evaluated in the principal-value sense. The dynamic condition in the inverse plane is the same as in the infinite-depth case (see Eq. (4.10) in Guyenne and Părău, 2012). A typical resolution $\Delta\Phi=0.025$ is used in the quadrature of (50). For free solitary waves, $P=0$ in the steady version of (47).

Thanks to the hodograph transformation, this numerical method can handle multivalued solutions. However, it is especially designed for computing solitary waves and thus is not suitable for periodic waves in general.

4.2. High-order spectral method for unsteady waves

To compute unsteady waves, we solve directly the Hamiltonian equations (8) and (9) in space and time (Craig and Sulem, 1993; Guyenne and Nicholls, 2007). For space discretisation, we assume periodic boundary conditions in x, with $0\le x\le L$, and use a pseudospectral method based on the fast Fourier transform. This is a particularly suitable choice for the computation of the DNO since each term in its Taylor series expansion (12)–(14) consists of concatenations of Fourier multipliers with powers of η.

More specifically, both functions η and ξ are expanded in truncated Fourier series

$$\begin{pmatrix}\eta\\ \xi\end{pmatrix}=\sum_k\begin{pmatrix}\widehat{\eta}_k\\ \widehat{\xi}_k\end{pmatrix}\mathrm{e}^{\mathrm{i}kx}.$$

Spatial derivatives and Fourier multipliers are evaluated in the Fourier domain, while nonlinear products are calculated in the physical domain on a regular grid of N collocation points. In practice, the Taylor series of the DNO is also truncated to a finite number of terms,

$$G(\eta)\approx\sum_{j=0}^{J}G_j(\eta), \tag{51}$$

and thanks to its analyticity properties, a small number of terms (typically $J<10$) is sufficient to achieve very accurate results (Xu and Guyenne, 2009).

Time integration of (8) and (9) is performed in the Fourier domain so that the linear terms can be solved exactly by the integrating factor technique. The nonlinear terms are integrated in time using a 4th-order Runge–Kutta scheme with constant time step Δt. Further details can be found in Xu and Guyenne (2009).

Starting from zero initial conditions, free solitary waves are produced by applying the pressure

$$P=P_0\mathrm{e}^{-(x-x_0-ct)^2/16}, \tag{52}$$

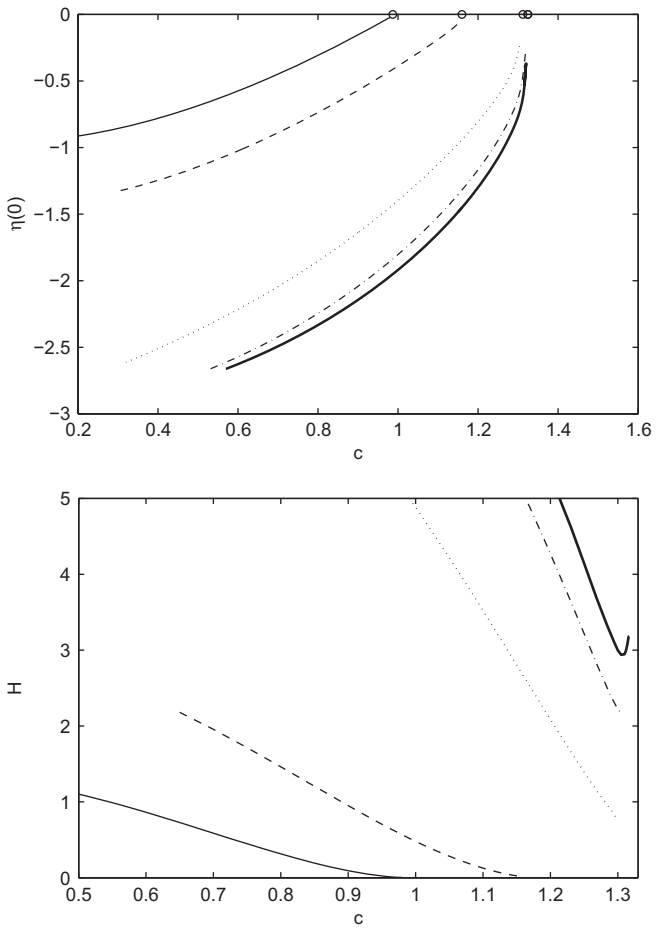

Fig. 3. Amplitudes (top figure) and energy (bottom figure) of depression solitary waves for $h=1$ (thin solid line), $h=1.5$ (dashed line), $h=3.095$ (dotted line), $h=5$ (dashed-dotted line) and $h=8$ (thick solid line). The critical speed $c_{\min}$ in each case is represented by a circle.

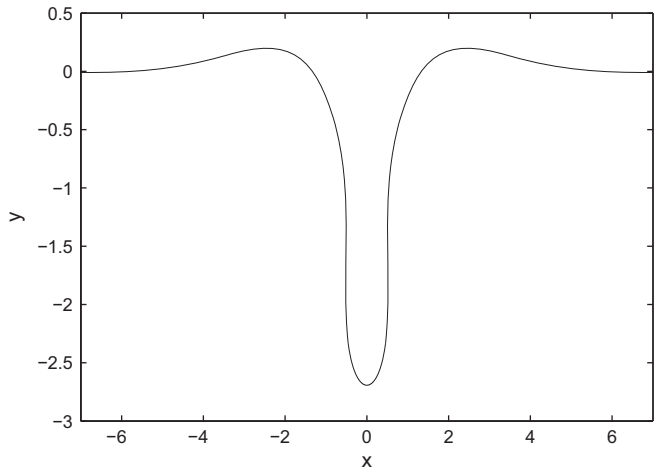

Fig. 4. Large-amplitude overturning solitary wave for $c=1.273$ and $h=3.095$. Only the central part of the wave is shown.

over a finite interval of time $0 \le t \le T$, with given P_0 and c ($T=125$ is chosen in all of our time-dependent simulations). The pressure distribution is initially centred at $x_0 = L/2$. To minimise the generation of radiation due to a cold start, we also apply a tanh-like ramp function in time to (52), which allows for a smooth transition from 0 to P_0 (Guyenne and Nicholls, 2007). Despite our effort however, small radiative waves were inevitably excited by the applied pressure in our numerical

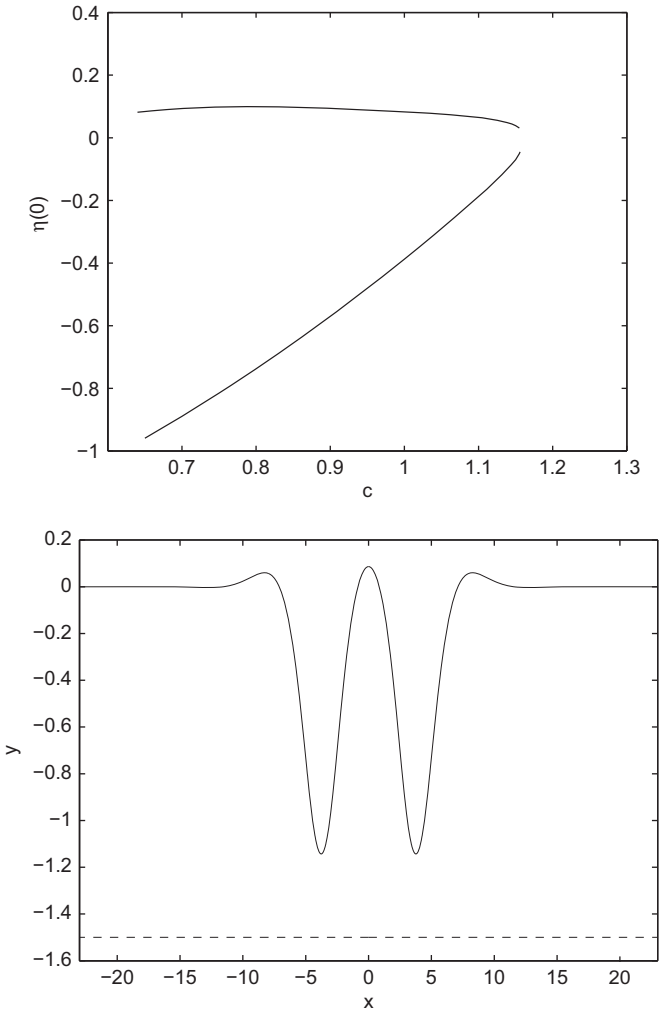

Fig. 5. Top figure: Branches of depression ($\eta(0)<0$) and elevation ($\eta(0)>0$) solitary waves for $h=1.5$. The corresponding critical speed is $c_{\min}=1.16$. Bottom figure: Profile of an elevation solitary wave for $c=0.5$ and $h=1.5$. The fluid depth is represented by a dashed line.

simulations. A typical run uses $J=6$, $\Delta t=0.002$ and $N=4096$ for a computational domain of length $L=600$. These values of numerical parameters were found to be a good compromise between accuracy and computational cost. In particular, the domain was specified long enough so that the numerical solution is not significantly affected by the periodic boundary conditions. Numerical tests on the conservation of invariants of motion will be shown in the next section.

Note that the Hamiltonian formulation (8) and (9) together with the series expansion (12)–(14) of the DNO require that η be a single-valued graph of x. Therefore, the multivalued solutions discussed below were not simulated in time.

5. Numerical results

The main purpose of this section is to compute both steady and unsteady solutions of the full equations, and compare with weakly nonlinear predictions from the NLS and 5th-order KdV equations. Steady waves are primarily compared with NLS solutions, while unsteady waves are primarily compared with 5th-order KdV solutions. Since our focus is on (stable) solitary waves, the NLS predictions are most relevant in the range $c<c_{\min}$, while the 5th-order KdV predictions are most relevant in the range $c>c_0$. Time-dependent simulations are also used to investigate the stability of solitary waves. Particular attention is paid to the case $h=3.095$ corresponding to Lake Saroma experiments (Takizawa, 1985).

5.1. Steady waves for $c<c_{\min}$

We first compute solitary waves in infinite depth for $c<c_{\min}$ as in Guyenne and Părău (2012) and then, by continuation, decrease the depth h. Depression and elevation solitary waves were found in all cases considered, as in infinite depth. In the latter setting, the full branches of depression and elevation solitary waves were recently computed by Wang et al. (2013).

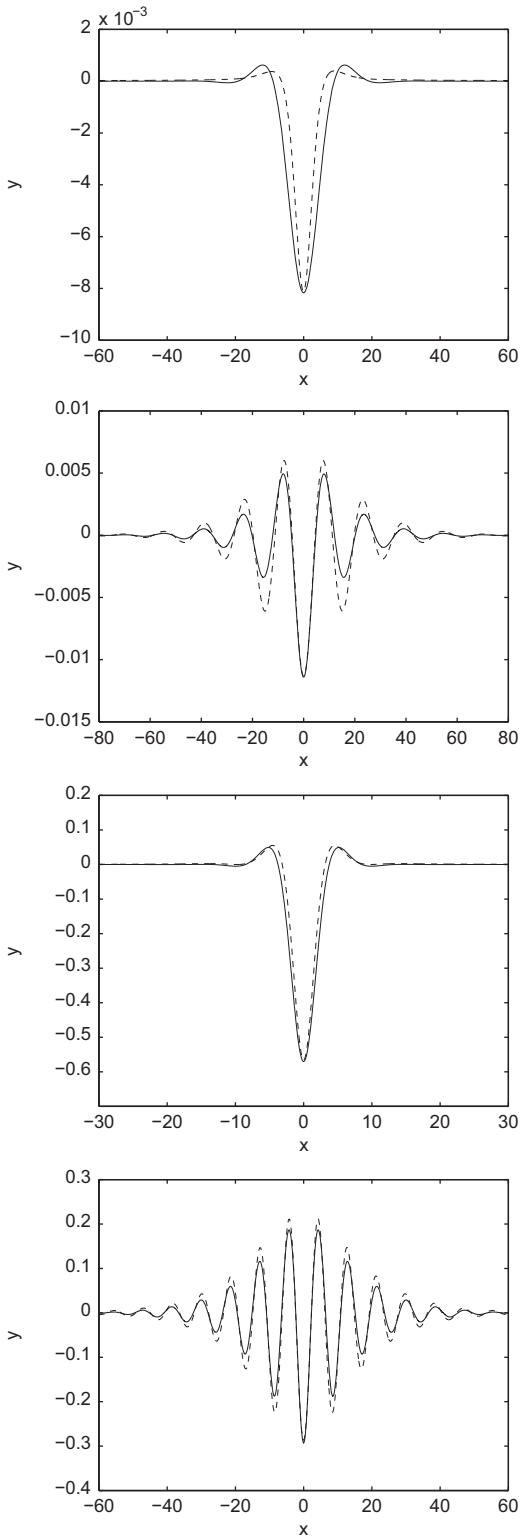

Fig. 6. Comparison of steady wave profiles obtained from the boundary-integral method (solid line) and the NLS soliton (44) (dashed line) for different parameter values: $(c,h)=(0.7,0.5)$, $(0.985,1)$, $(0.9,1.5)$ and $(1.3,3.095)$ (from top to bottom).

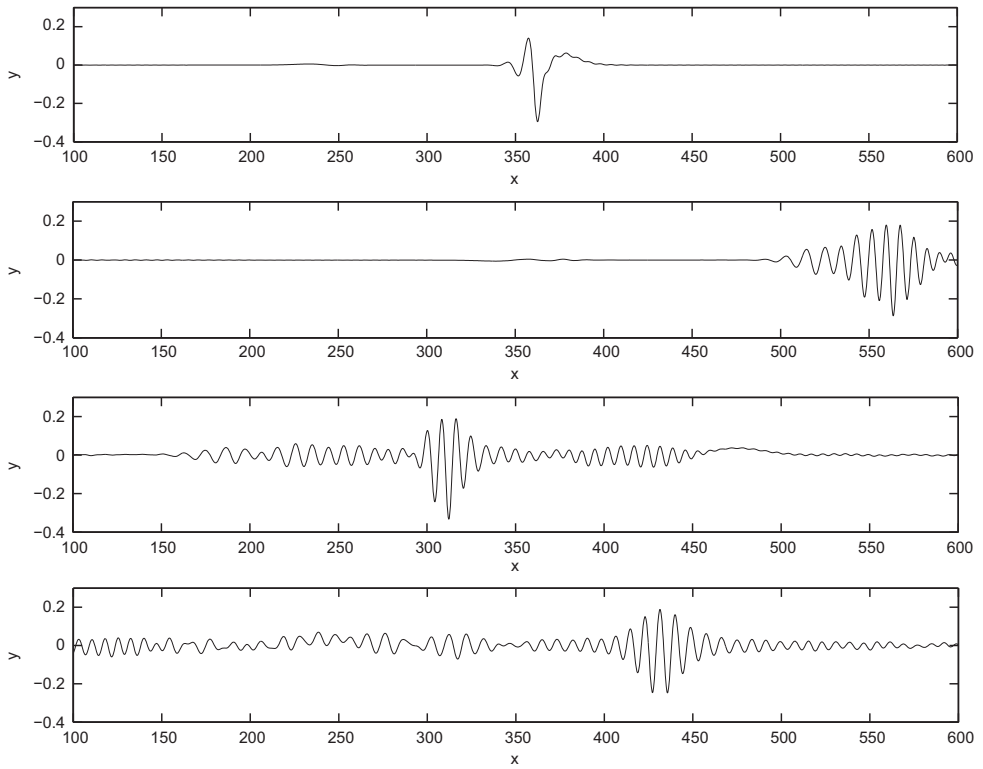

Fig. 7. Snapshots of the ice-sheet deflection $\eta(x,t)$ at $t=50$, 200, 450, 1000 (from top to bottom) for $P_0=0.045$, $c=1.302$ and $h=3.095$. The pressure is removed at $t=125$.

Amplitude branches of depression solitary waves are presented in Fig. 3 for different values of h. For $h=8$, the branch is very close to that in infinite depth and starts from a nonzero finite amplitude at $c=c_{\min}$. However, for $h=1$ and $h=1.5$, the wave amplitudes seem to approach zero at $c=c_{\min}$. Therefore, in shallow water, the solitary wave branches seem to start from zero amplitude while, in deeper water, they start at a finite amplitude. The exact critical depth where this change occurs cannot be easily found as it is difficult to accurately compute waves for values of c very close to $c_{\min}$ (more and more oscillations appear and an increasingly larger number of grid points is needed). We estimate this critical depth to be near $h=2$, which is smaller than the critical depth $h_c=8.773$ where the cubic coefficient μ of the NLS equation (39) changes sign.

In Fig. 4, we present a large-amplitude solitary wave with slightly overturning profile for $h=3.095$. Such waves are found when c is small and for moderate to large depth. In infinite depth, we showed that the limiting case $c=0$ gives rise to a self-intersecting wave profile of amplitude 2.83, which is clearly unphysical (Guyenne and Părău, 2012). For large depth, the branch of depression solitary waves approaches a similar limiting profile. However, we were not able to follow this branch down to $c=0$ because our solutions need to satisfy $x'(\phi)\to 1/c$ as $\phi\to\infty$, and thus the numerical scheme fails to yield accurate results for very small values of c.

A different behaviour is observed for small depth, in particular, smaller than this limiting amplitude of 2.83. In this case, the solutions are bounded by h and cannot approach the limiting solution (see Fig. 3). We did not observe solutions with overturning profiles for small values of h (e.g. $h=1$).

Another interesting feature is revealed when the energy

$$H=-\frac{1}{2}c\int_{-\infty}^{\infty} y\,d\Phi+\frac{1}{2}\int_{-\infty}^{\infty} y^2x'\,d\Phi+\frac{1}{2}\int_{-\infty}^{\infty}\frac{(y''x'-x''y')^2}{(x'^2+y'^2)^{5/2}}\,d\Phi \tag{53}$$

is plotted as a function of c (Fig. 3). In infinite depth, we found that the energy has a minimum at about $c_m=1.31$. This minimum is still observed for large values of h (e.g. $h=8$) but it disappears as h decreases. The absence of extrema in the energy for $h<8$ is consistent with the NLS predictions and time-dependent numerical simulations (as described in the next section) which indicate that solitary waves of depression are stable in shallow water.

Branches of depression and elevation solitary waves are plotted in Fig. 5 for $h=1.5$. We see that the elevation branch is not uniformly increasing with decreasing c, and its amplitude remains relatively small. However, for a given c, the troughs near the central crest of elevation solitary waves are of the same amplitude as the corresponding solitary waves of depression.

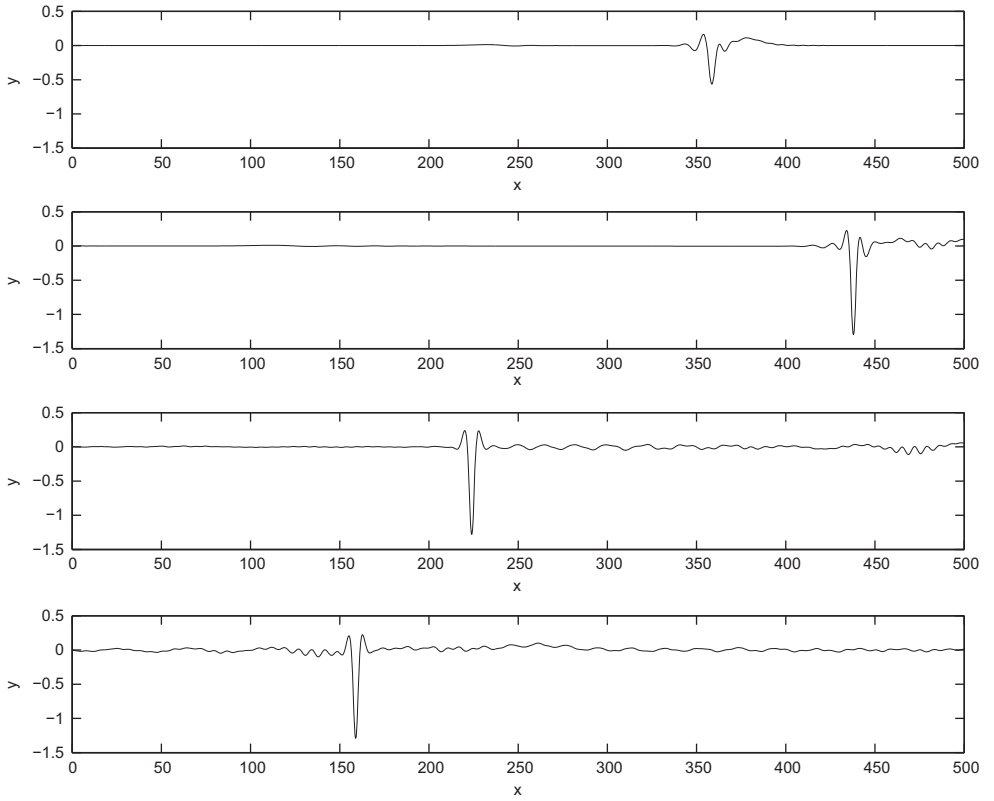

Fig. 8. Snapshots of the ice-sheet deflection $\eta(x,t)$ at $t=50$, 120, 490, 1000 (from top to bottom) for $P_0=0.1$, $c=1.056$ and $h=3.095$. The pressure is removed at $t=125$.

Both branches start from zero amplitude at $c=c_{\min}$. Their amplitudes are comparable with the fluid depth when c is far away from $c_{\min}$, as indicated by the profile of an elevation solitary wave in Fig. 5.

Fig. 6 shows a direct comparison of steady wave profiles obtained from the boundary-integral method and from (43) together with the NLS soliton (44), for various values of c and h. Here $k_0=k_{\min}$ is dependent on h and determined numerically by equating the group and phase velocities, $\omega_k=\omega/k$ (see Section 2.4). For convenience, we set $\varepsilon=1$ and only vary u_0 in (43) and (44) to fit the fully nonlinear solution as closely as possible, which implies that wave steepness is now measured by the parameter u_0. Overall, there is a good agreement, especially regarding the relative amplitude of the central trough and the wavelength. For e.g. $h=3.095$, we find $k_{\min}=0.735$ and it can be graphically checked in Fig. 6 that the wavelength (i.e. the distance between two consecutive crests) is about $\ell_{\min}=2\pi/k_{\min}=8.548$. The NLS prediction is able to capture well the main features, whether the solution is a localised or broader solitary wavepacket. This confirms in particular that the inclusion of the mean component $\tilde{\eta}_1$ in (43) is crucial at reproducing well the vertical asymmetry of the solution. As stated in Section 3.2.4, we see that the agreement slowly deteriorates as h decreases.

5.2. Unsteady waves

We first examine the regime $c<c_{\min}$ for $h=3.095$. When a very small pressure P_0 is applied, the linear effects prevail and so the initial localised disturbance quickly spreads out after the forcing is removed at $t=T=125$. However, as P_0 is increased (say $P_0=0.045$ with $c=1.302$), the solution evolves into a small-amplitude solitary wavepacket resembling that in Fig. 6 but coexisting with significant background radiation. This wavepacket travels from left to right and seems to persist at least up to $t=1000$ (Fig. 7). A larger-amplitude and more localised solitary wave of depression propagating at speed $c=1.056$ with near-constant shape is obtained for $P_0=0.1$, as depicted in Fig. 8. Radiative waves are still noticeable but are significantly smaller than the main pulse. These results confirm the NLS analysis in Section 3.2.4 that small- and even large-amplitude solitary waves (of depression) are stable. Similar behaviours were observed for smaller values of h in this regime. As pointed out in Guyenne and Părău (2012) for infinite depth, some relaxation typically occurs so that the actual speed of the solitary wave measured after $t=T$ is not exactly equal, but close, to the speed initially set by the applied pressure. For convenience, in the case of stable or long-lived solitary waves, we only report the actual wave speed c.

In Guyenne and Părău (2012), direct comparisons were made between results by the boundary-integral and high-order spectral methods, giving us confidence on the accuracy of these two independent algorithms. Because the present schemes are

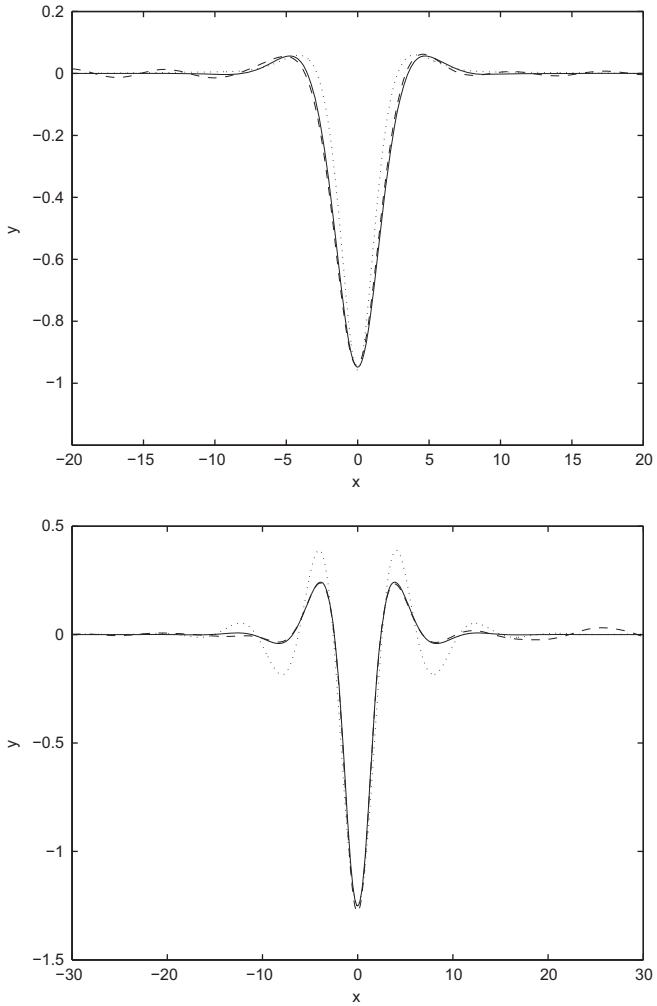

Fig. 9. Comparison of wave profiles obtained from the boundary-integral method (solid line), the high-order spectral method (dashed line) and the NLS soliton (44) (dotted line) at $t=490$ for $(c,h)=(0.658,1.5)$ (top figure) and $(1.056,3.095)$ (bottom figure).

similar to those described in Guyenne and Părău (2012), we only show two further comparisons in the finite-depth case for completeness. Fig. 9 displays the superposition of steady and unsteady wave profiles computed by our two numerical methods, for $(c,h)=(0.658,1.5)$ and $(1.056,3.095)$ at $t=490>T$. We choose two cases of well-localised solitary waves of depression which stably propagate for $t>T$ in our time-dependent simulations. We again find an excellent agreement, with small discrepancies at the wave tails which are attributable to unsteadiness caused by interaction with the background radiation. NLS solutions are also plotted in Fig. 9 and, surprisingly, they still approximate the wave profile reasonably well, even for such large amplitudes (relative to h).

Although steady solutions show the existence of elevation solitary waves (see Fig. 5), we were not able to reproduce such waves with our time-dependent algorithm, which suggests that they are unstable. Indeed, for large (negative) pressure amplitudes, the initial hump evolves instead into a stable solitary wave of depression, thus further supporting the fact that solitary waves of depression are stable for $c<c_{\min}$. The same scenario was found to occur in infinite depth (Guyenne and Părău, 2012).

We now turn our attention to the regime $c>c_0$. For $h=3.095$ and $P_0=0.1$, a solitary wave of elevation emerges in Fig. 10, which tends to separate at speed $c=1.905$ from a large-scale radiative wavepacket induced by the initial forcing. Incidentally, a similar solution would develop if a negative pressure $P_0=-0.1$ were applied. A close-up of this solitary wave of elevation is presented in Fig. 11 which compares it with a (numerical) solitary wave solution of the 5th-order KdV equation (21). We again set $\varepsilon=1$ and only vary σ in (22)–(24) so that the iterative solution of (23) fits the fully nonlinear solitary wave as closely as possible. As in the context of gravity (or gravity-capillary) water waves, these 5th-order KdV solutions are so-called 'generalised' solitary waves in the sense that they are not truly localised but their central pulse typically connects to smaller periodic waves on both sides, as found in steady computations of Champneys et al. (2002).

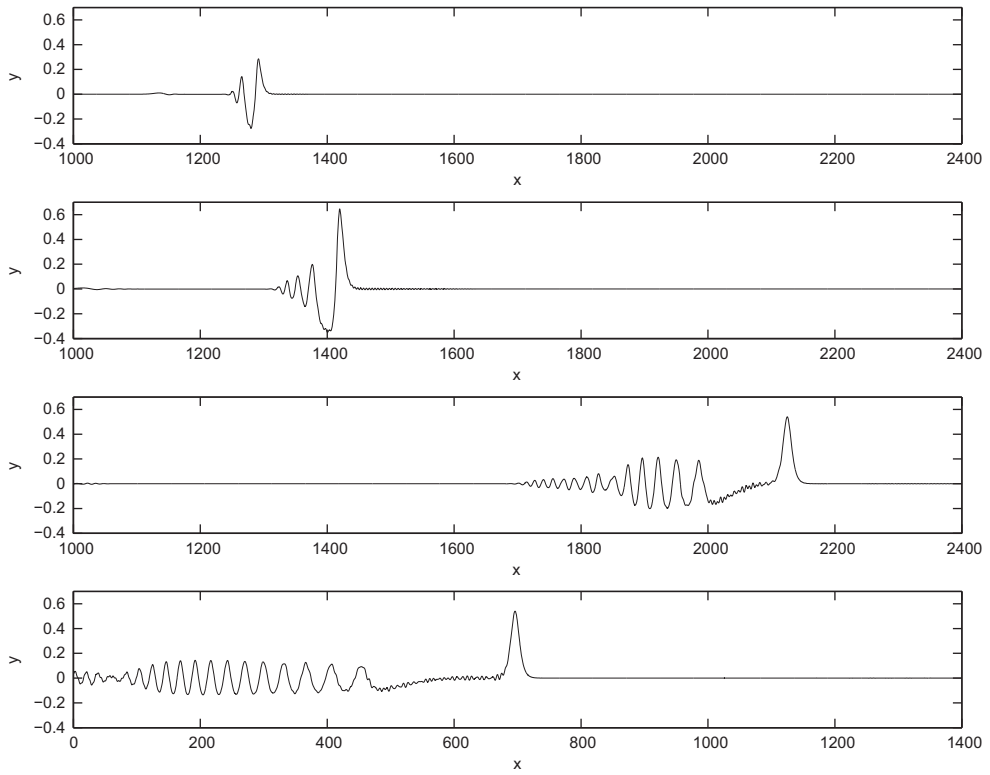

Fig. 10. Snapshots of the ice-sheet deflection $\eta(x,t)$ at $t=50$, 120, 490, 1000 (from top to bottom) for $P_0=0.1$, $c=1.905$ and $h=3.095$. The pressure is removed at $t=125$.

The wavelength $\ell_d=2\pi/k_d$ of these dispersive tails is determined by the resonance condition

$$c_d(k_d)=\sqrt{h}\left[1-\frac{1}{6}h^2k_d^2+\left(\frac{19}{360}h^4+\frac{1}{2}\right)k_d^4\right]=c, \tag{54}$$

where c_d is the 5th-order KdV approximation of (15) in dimensionless units. Solving (54) numerically yields $k_d=0.586$ for e.g. $(c,h)=(1.905,3.095)$, and it can be graphically checked in Fig. 11 that the dispersive wavelength is about $\ell_d=2\pi/k_d=10.714$ on both sides of the 5th-order KdV solitary wave. Fig. 11 indicates a very good agreement for the central pulse in both amplitude and width. However, the fully nonlinear solitary wave seems to exhibit only one dispersive tail trailing behind it (i.e. on its left side). Despite the irregular unsteady shape of this dispersive tail, we see that its wavelength and amplitude are comparable to those in the 5th-order KdV solution. Such a low level of radiation may explain why this solitary wave of elevation seems to be steadily progressing, at least up to $t=1000$. However, it is likely to be unstable as it gradually loses energy by emitting radiation (Michallet and Dias, 1999).

As far as unsteady solutions are concerned, the occurrence of two dispersive tails is not possible in the present conservative case because otherwise this would imply that there is a wave source/sink at either $+\infty$ or $-\infty$. As mentioned in Michallet and Dias (1999), on which side the dispersive tail appears is determined by the value of its group velocity relative to that of its phase velocity. If the group velocity is less than the phase velocity, then ripples appear behind the solitary pulse. Otherwise, they appear ahead of it. In the present hydroelastic problem, the group velocity is less than the phase velocity if $k<k_{\min}$ and larger otherwise. Therefore, since $k_d=0.586<k_{\min}=0.735$ for $(c,h)=(1.905,3.095)$, ripples should trail behind the main pulse (i.e. on its left side), which is confirmed in Fig. 11.

On the other hand, for shallower water, say $(c,h)=(0.722,0.5)$, we find $k_d=0.501>k_{\min}=0.204$ and thus ripples are emitted ahead of the main crest (i.e. on its right side), as shown in Fig. 11. In this case again, the agreement is overall satisfactory between the 5th-order KdV and fully nonlinear solutions, modulo discrepancies due to unsteadiness in the latter. However, the fully nonlinear wave disperses more quickly than in the previous situation $h=3.095$ because it emits a higher level of radiation. Note that the trough on the left side of the main crest is a remnant of the initial disturbance induced by the applied pressure (with $P_0=0.01$).

Finally, the conservation of the invariants of motion (i.e. energy H, impulse I and volume V) after $t=T$ is illustrated in Fig. 12, for $(c,h)=(1.056,3.095)$ and $(1.905,3.095)$. In both cases, we observe that these quantities are all very well conserved in time, with V being essentially zero as in the infinite-depth limit (Longuet-Higgins, 1989; Guyenne and Părău, 2012).

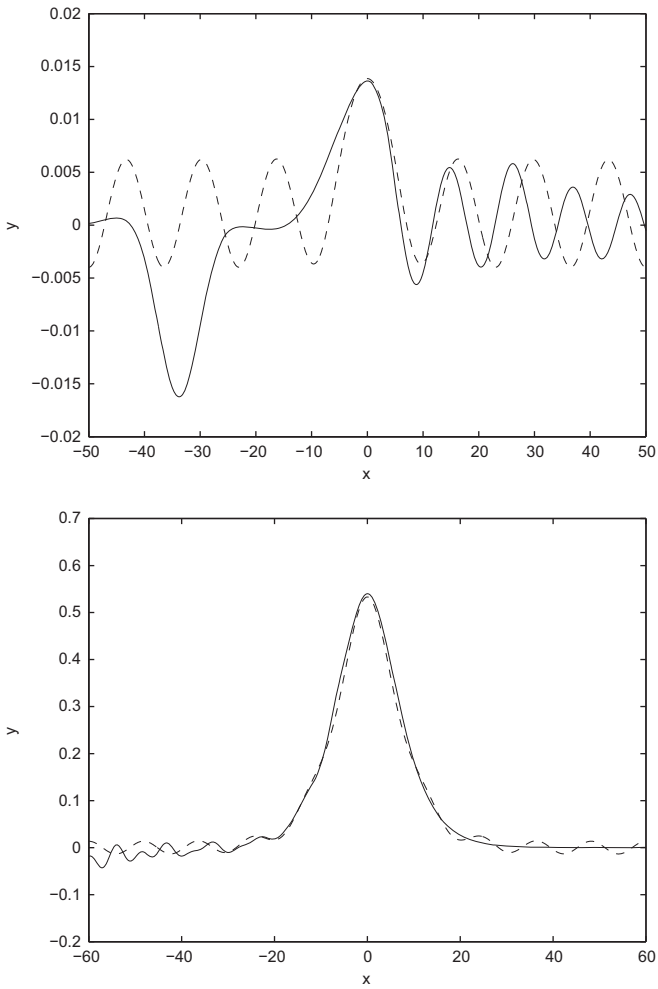

Fig. 11. Comparison of wave profiles obtained from the high-order spectral method (solid line) and from the 5th-order KdV equation (21) (dashed line) at $t=140$ for $(c,h)=(0.722,0.5)$ (top figure) and at $t=490$ for $(c,h)=(1.905,3.095)$ (bottom figure).

Comparing Figs. 3 and 12, we notice that the energy values for $(c,h)=(1.056,3.095)$ from the boundary-integral and high-order spectral computations are both close to $H=4$.

6. Conclusions

Two-dimensional nonlinear flexural-gravity waves propagating at the surface of a finite-depth fluid covered by an ice sheet are investigated. The ice cover is modelled as a thin elastic sheet, based on the special Cosserat theory for hyperelastic shells as proposed by Plotnikov and Toland (2011). After transformation to Hamiltonian variables, weakly nonlinear wave models are derived in the modulational and long-wave regimes, including a cubic NLS equation for wave speeds c near the minimum phase velocity $c_{\min}$ and a 5th-order KdV equation for c near the long-wave limit c_0. A critical depth h_c, where the cubic coefficient of the NLS equation changes sign, implies that soliton solutions exist and are stable for depth $h<h_c$. A similar critical depth was found by Părău and Dias (2002) for a related ice-sheet model.

For the full nonlinear problem, in the regime $c<c_{\min}$, both depression and elevation solitary waves are computed numerically over a wide range of depths. These solutions bifurcate from a nonzero finite amplitude when h is large, similar to the infinite-depth case (Guyenne and Părău, 2012), while they seem to start from zero amplitude when h is small. Overturning waves of depression are also found for low wave speeds and sufficiently large depth. Our time-dependent simulations confirm that small- to large-amplitude solitary waves of depression are stable. Solitary waves of elevation however seem to be unstable in all cases, including $c>c_0$ where they resemble generalised solitary wave solutions of our 5th-order KdV equation. Such waves radiate energy and thus decay in time.

In the future, it would be of interest to investigate the three-dimensional problem both theoretically and numerically within the Hamiltonian framework to complement the weakly nonlinear results of Milewski and Wang (2013). Preliminary

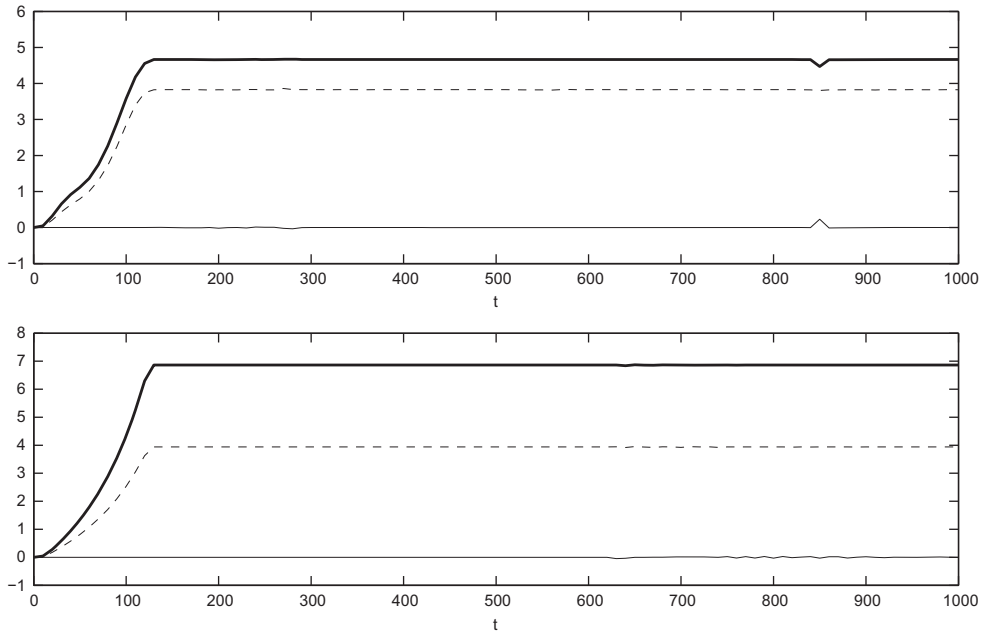

Fig. 12. Time evolution of energy H (thick solid line), impulse I (dashed line) and volume V (thin solid line) for $(c,h)=(1.056,3.095)$ (top) and $(1.905,3.095)$ (bottom). The pressure is removed at $t=125$.

three-dimensional computations were performed by Părău and Vanden-Broeck (2011) for a linear Euler–Bernoulli model of the ice sheet combined with nonlinear potential flow.

Acknowledgments

P. Guyenne is partially supported by the Simons Foundation under grant 246170. E.I. Părău is supported by the EPSRC under grant EP/J019305/1.

References

Akylas, T.R., 1993. Envelope solitons with stationary crests. Physics of Fluids 5, 789–791.
Bonnefoy, F., Meylan, M.H., Ferrant, P., 2009. Nonlinear higher-order spectral solution for a two-dimensional moving load on ice. Journal of Fluid Mechanics 621, 215–242.
Champneys, A.R., Vanden-Broeck, J.-M., Lord, G.J., 2002. Do true elevation gravity-capillary solitary waves exist? A numerical investigation. Journal of Fluid Mechanics 454, 403–417.
Craig, W., Groves, M.D., 1994. Hamiltonian long-wave approximations to the water-wave problem. Wave Motion 19, 367–389.
Craig, W., Guyenne, P., Kalisch, H., 2005a. Hamiltonian long wave expansions for free surfaces and interfaces. Communications on Pure and Applied Mathematics 58, 1587–1641.
Craig, W., Guyenne, P., Nicholls, D.P., Sulem, C., 2005b. Hamiltonian long-wave expansions for water waves over a rough bottom. Proceedings of the Royal Society A 461, 839–873.
Craig, W., Guyenne, P., Sulem, C., 2010. A Hamiltonian approach to nonlinear modulation of surface water waves. Wave Motion 47, 552–563.
Craig, W., Guyenne, P., Sulem, C., 2012. Hamiltonian higher-order nonlinear Schrödinger equations for broader-banded waves on deep water. European Journal of Mechanics B/Fluids 32, 22–31.
Craig, W., Schanz, U., Sulem, C., 1997. The modulational regime of three-dimensional water waves and the Davey–Stewartson system. Annales de l'Institut Henri Poincaré (C) Non Linear Analysis 14, 615–667.
Craig, W., Sulem, C., 1993. Numerical simulation of gravity waves. Journal of Computational Physics 108, 73–83.
Forbes, L.K., 1986. Surface-waves of large amplitude beneath an elastic sheet. Part 1. High-order solutions. Journal of Fluid Mechanics 169, 409–428.
Grillakis, M., Shatah, J., Strauss, W., 1987. Stability theory of solitary waves in the presence of symmetry. I. Journal of Functional Analysis 74, 160–197.
Guyenne, P., Nicholls, D.P., 2007. A high-order spectral method for nonlinear water waves over moving bottom topography. SIAM Journal on Scientific Computing 30, 81–101.
Guyenne, P., Părău, E.I., 2012. Computations of fully nonlinear hydroelastic solitary waves on deep water. Journal of Fluid Mechanics 713, 307–329.
Haragus-Courcelle, M., Ilichev, A., 1998. Three-dimensional solitary waves in the presence of additional surface effects. European Journal of Mechanics B/Fluids 17, 739–768.
Hegarty, G.M., Squire, V.A., 2008. A boundary-integral method for the interaction of large-amplitude ocean waves with a compliant floating raft such as a sea-ice floe. Journal of Engineering Mathematics 62, 355–372.
Kaup, D.J., 1975. A higher-order wave equation and the method for solving it. Progress of Theoretical Physics 54, 396–408.
Korobkin, A., Părău, E.I., Vanden-Broeck, J.-M., 2011. The mathematical challenges and modelling of hydroelasticity. Philosophical Transactions of the Royal Society A: Physical, Mathematical and Engineering Sciences 369, 2803–2812.
Longuet-Higgins, M.S., 1989. Capillary-gravity waves of solitary type on deep water. Journal of Fluid Mechanics 200, 451–470.
Marko, J.R., 2003. Observations and analyses of an intense waves-in-ice event in the Sea of Okhotsk. Journal of Geophysical Research 108, 3296.
Meylan, M., Sturova, I., 2009. Time-dependent motion of a two-dimensional floating elastic plate. Journal of Fluids and Structures 25, 445–460.

Michallet, H., Dias, F., 1999. Numerical study of generalized interfacial solitary waves. Physics of Fluids 11, 1502–1511.
Milewski, P.A., Vanden-Broeck, J.-M., Wang, Z., 2011. Hydroelastic solitary waves in deep water. Journal of Fluid Mechanics 679, 628–640.
Milewski, P.A., Wang, Z., 2013. Three dimensional flexural-gravity waves. Studies in Applied Mathematics 131, 135–148.
Mohapatra, S., Ghoshal, R., Sahoo, T., 2013. Effect of compression on wave diffraction by a floating elastic plate. Journal of Fluids and Structures 36, 124–135.
Montiel, F., Bennetts, L., Squire, V., 2012. The transient response of floating elastic plates to wavemaker forcing in two dimensions. Journal of Fluids and Structures 28, 416–433.
Plotnikov, P.I., Toland, J.F., 2011. Modelling nonlinear hydroelastic waves. Philosophical Transactions of the Royal Society A: Physical, Mathematical and Engineering Sciences 369, 2942–2956.
Părău, E., Dias, F., 2002. Nonlinear effects in the response of a floating ice plate to a moving load. Journal of Fluid Mechanics 460, 281–305.
Părău, E.I., Vanden-Broeck, J.-M., 2011. Three-dimensional waves beneath an ice sheet due to a steadily moving pressure. Philosophical Transactions of the Royal Society A: Physical, Mathematical and Engineering Sciences 369, 2973–2988.
Schulkes, R.M.S.M., Hosking, R.J., Sneyd, A.D., 1987. Waves due to a steadily moving source on a floating ice plate. Part 2. Journal of Fluid Mechanics 180, 297–318.
Squire, V.A., 2011. Past, present and impendent hydroelastic challenges in the polar and subpolar seas. Philosophical Transactions of the Royal Society A: Physical, Mathematical and Engineering Sciences 369, 2813–2831.
Squire, V.A., Hosking, R.J., Kerr, A.D., Langhorne, P.J., 1996. Moving Loads on Ice Plates. Kluwer, Dordrecht.
Takizawa, T., 1985. Deflection of a floating sea ice sheet induced by a moving load. Cold Regions Science and Technology 11, 171–180.
Vanden-Broeck, J.-M., Părău, E.I., 2011. Two-dimensional generalised solitary waves and periodic waves under an ice sheet. Philosophical Transactions of the Royal Society A: Physical, Mathematical and Engineering Sciences 369, 2957–2972.
Wang, Z., Vanden-Broeck, J.-M., Milewski, P.A., 2013. Two-dimensional flexural-gravity waves of finite amplitude in deep water. IMA Journal of Applied Mathematics 78, 750–761.
Xia, X., Shen, H.T., 2002. Nonlinear interaction of ice cover with shallow water waves in channels. Journal of Fluid Mechanics 467, 259–268.
Xu, L., Guyenne, P., 2009. Numerical simulation of three-dimensional nonlinear water waves. Journal of Computational Physics 228, 8446–8466.
Zakharov, V.E., 1968. Stability of periodic waves of finite amplitude on the surface of a deep fluid. Journal of Applied Mechanics and Technical Physics 9, 190–194.